Reachable Workspace and Proximal Function Measures for Quantifying Upper Limb Motion

Robert P. Matthew, Sarah Seko, Gregorij Kurillo, Ruzena Bajcsy, Louis Cheng, Jay J. Han, and Jeffrey Lotz

***Abstract*—There are a lack of quantitative measures for clinically assessing upper limb function. Conventional biomechanical performance measures are restricted to specialist labs due to hardware cost and complexity, while the resulting measurements require specialists for analysis. Depth cameras are low cost and portable systems that can track surrogate joint positions. However, these motions may not be biologically consistent, which can result in noisy, inaccurate movements. This paper introduces a rigid body modelling method to enforce biological feasibility of the recovered motions. This method is evaluated on an existing depth camera assessment: the reachable workspace (RW) measure for assessing gross shoulder function. As a rigid body model is used, position estimates of new proximal targets can be added, resulting in a proximal function (PF) measure for assessing a subject's ability to touch specific body landmarks. The accuracy, and repeatability of these measures is assessed on ten asymptomatic subjects, with and without rigid body constraints. This analysis is performed both on a low-cost depth camera system and a gold-standard active motion capture system. The addition of rigid body constraints was found to improve accuracy and concordance of the depth camera system, particularly in lateral reaching movements. Both RW and PF measures were found to be feasible candidates for clinical assessment, with future analysis needed to determine their ability to detect changes within specific patient populations.**

***Index Terms*—Depth camera, upper limb, clinical metrics, quantitative, range of motion, functional assessment, rigid body modelling.**

Manuscript received October 30, 2019; revised February 27, 2020; accepted April 16, 2020. Date of publication April 23, 2020; date of current version November 5, 2020. This work was supported by the UCSF Department of Orthopaedic Surgery. *(Corresponding author: Robert Matthew.)*

Robert P. Matthew is with the Department of Physical Therapy and Rehabilitation Science, University of California at San Francisco, San Francisco, CA 94158 USA (e-mail: robert.matthew@ucsf.edu).

Sarah Seko and Ruzena Bajcsy are with the Department of Electrical Engineering, University of California at Berkeley, Berkeley, CA 94720 USA (e-mail: seko@berkeley.edu; bajcsy@berkeley.edu).

Gregorij Kurillo and Jeffrey Lotz are with the Department of Orthopaedic Surgery, University of California at San Francisco, Orange, CA 94158 USA (e-mail: Gregorij.Kurillo@ucsf.edu; Jeffrey.Lotz@ucsf.edu).

Louis Cheng is with the Bioniks, Alameda, CA 94501 USA (e-mail: lcheng@bioniks.net).

Jay J. Han is with the Department of Physical Medicine & Rehabilitation, UC Irvine School of Medicine, San Francisco, CA 92868 USA (e-mail: jayjhan@hs.uci.edu).

Digital Object Identifier 10.1109/JBHI.2020.2989722

I. Introduction

ACCURATE and repeatable measures of human performance are essential for tracking patient outcomes and determining the efficacy of interventions. While highly accurate methods for assessing an individual's movement exist, these methods typically require access to a specialised biomechanics lab. The requirements for costly hardware, dedicated space for setting up motion-capture cameras, and specialists needed to collect and process this data are limiting factors that hinders the use of these methods as part of standard patient care.

Existing clinical measurements instead focus on single joint goniometry or task-specific scores. Some tests, such as the Functional Independence measure and Fugl-Meyer assessment, provide a point score based on the degree of assistance needed during a set of daily living tasks. While these tests are easily deployable in clinic, able to track function, have excellent inter-rater reliability, and are highly recommended by professional organisations [1]–[3], they are unable to distinguish between compensation and true recovery [4]. Functional testing rarely provides measures of compensation or movement synergies. Instead these methods are scored based on task completion or a subjective binary assessment of perceived difficulty. This results in insufficient resolution to distinguish between varying levels of function and may confound improvement with the adoption of a potentially undesirable compensatory mechanism.

This is in contrast to the traditional model based approach used in biomechanics [5]. High accuracy measurements of motion capture markers can be obtained through television (i.e. Vicon), optoelectric (i.e. OptoTrack), or magnetic (i.e. Ascension) methods. By placing these markers on specific anatomical landmarks, a rigid body model can be used to estimate the corresponding limb pose. Joint centre locations can be inferred from the relative locations of markers or through the use of function recovery and optimisation methods [6], [7]. This allows for the study of compound motions of the sternum, clavicle and humerus during arm motion [8] and the quantification of movement during activity [9]. These methods are the gold standard for biomechanics research, whose accuracy is only surpassed by methods such as bi-planar fluoroscopy [10].

Depth camera systems can be used as an alternative method for obtaining 3D joint positions. Popularised by the Microsoft Kinect, there are a number of commercial depth camera systems including the Intel RealSense, VicoVR, Depthsense, PMD, and SICK. These cameras estimate the depth of each image pixel by projecting either known patterns onto the environment

(structured light), from a scanned point (time of flight), or triangulation [11]. This depth image can be converted into an estimated skeletal pose natively, or can be combined with a skeletal tracking library such as Nuitrack or OpenNI. These libraries use a learned decoder that applies a pixel-wise labelling to each RGB-D pixel to identify limbs. The joint centres can then be estimated from the intersection of these limb segments [12]. This results in real-time frame-wise estimates of full-body pose.

Although the connections of the resulting skeleton are biologically-consistent, the lengths of the limbs and joint limits are not constrained, resulting in non-realistic movements [13]. These problems can be seen in cases of self-occlusion and cases where the subject is not facing the camera [11], or during periods of high speed movement [14]. The accuracy of the detected joint centres and corresponding angles is therefore dependent on the experimental motion protocol which is rarely standardised [11], [15]. This limits the use of this technique as a clinical assessment tool with a number of depth camera systems focusing on single joint assessment and coaching using video games [16].

In an effort to overcome some of these challenges, novel metrics and movement protocols have been introduced. Kurillo *et al.* proposed the *reachable workspace* measure for the assessment of shoulder function [17]. This method projects the motions of the wrist onto an allometrically scaled sphere centred at the shoulder. The area encompassed by the observed trajectories can be computed and used as a quantitative measure of shoulder function. The order of the arm movements and timing of each action is kept consistent between trials by using a coaching video which aids protocol consistency. This measure has seen success in the assessment of subjects with muscular dystrophy and amyotrophic lateral sclerosis and has been shown to correlate with other clinical measures [18]–[23]. While this test appears to be a promising measure, it is likely to be sensitive to the same variable limb-length issues.

One approach for improving the biological feasibility of the depth camera estimates is to combine frame-wise joint centre estimates from a depth camera with the traditional rigid body modelling approach. This approach has been used in the collection and analysis of sit-to-stand movements [24]. The kinematics and dynamics of this motion can be recovered, providing estimates of loading in the low-back and ground reaction forces [25]. This method of combining a depth camera system with a rigid body model and a fixed clinical protocol resulted in the identification of cohort specific variables of performance [26]. Patients with low back pain were found to move slower and with higher hip and spine loading when compared to control subjects. This difference was less pronounced post-surgery, suggesting that some of the identified measures are potentially useful for quantifying patient outcomes. Furthermore, this analysis was able to identify a single subject who later developed a post surgical complication (proximal joint fracture) before the fracture occurred. This suggests that these metrics may be able to identify early signs of complications before they result in mechanical failure.

A. Contributions

This paper assesses the feasibility and efficacy of combining depth cameras with rigid body models for upper limb clinical assessment. Two movement protocols are tested: the *reachable workspace* measure for assessing distal arm movement and the *proximal function* measure for assessing a subject's ability to reach specific body landmarks that are related to activities of daily living. The performance of the depth camera (*Kinect 2, Microsoft*) is compared to a gold-standard active motion capture system (*Impulse X2, Phasespace*). The effect of constraining the raw joint position estimates using an allometrically scaled rigid body model is examined for both the depth camera and baseline systems. Finally recommendations are given on the appropriateness of using depth camera systems for upper limb clinical assessment.

II. Methods

This section outlines an approach for correcting the non-biological movements seen in the raw depth camera skeleton and two proposed motions and measures for assessing upper limb performance. Section II-A introduces the rigid body modelling framework and a non-linear least squares approach to inverse kinematics. Two movement protocols are proposed in Section II-B, the *reachable workspace* (RW) for assessing gross range-of-motion and the *proximal function* (PF) for reaching body landmarks related to activities of daily living.

A. Models

To correct for non-biologically consistent movements, an allometrically scaled rigid body model is used (Section II-A1). Inman's model of scapulohumeral rhythm is incorporated into this model in Section II-A2 [27]. This rigid body model is used to estimate the corresponding joint angles and re-projected limb positions using framewise non-linear least squares optimisation (Section II-A3).

1) Rigid Body Modelling: The rigid body model consists of seven allometrically scaled segments which connect eight anatomical landmarks. The seven segments are separated into two serial chains for the left and right arms which originate at the torso. The torso is modelled as the base link of the system, with both scapulae rotating at a common torso origin.

The movement of the torso (T) in the world frame (W) is modelled as a floating system with the associated homogeneous transform:

$$\mathbf{g}_{W,T} = \begin{bmatrix} \mathbf{R}_{-X}\mathbf{R}_{+Y}\mathbf{R}_{+Z} & \mathbf{t} \\ \mathbf{0} & 1 \end{bmatrix} \tag{1}$$

where $\mathbf{t} \in \mathbb{R}^{3\times 1}$ is the translation from the world frame to the torso frame, and $\mathbf{R} \in \mathcal{SO}(3)$ are standard rotations in the special orthogonal group, each parameterised by angle θ.

The scapula (SC), upper arm (UA) and forearm (FA) are then modelled as two branches from the torso with the right arm modelled as:

$$\mathbf{g}_{T,RSC} = \begin{bmatrix} \mathbf{R}_{+Z}\mathbf{R}_{-Y} & \mathbf{0} \\ \mathbf{0} & 1 \end{bmatrix} \tag{2}$$

$$\mathbf{g}_{RSC,RUA} = \begin{bmatrix} \mathbf{R}_{+Z}\mathbf{R}_{-Y}\mathbf{R}_{+Z} & \mathbf{q_{RSJC}} \\ \mathbf{0} & 1 \end{bmatrix} \tag{3}$$

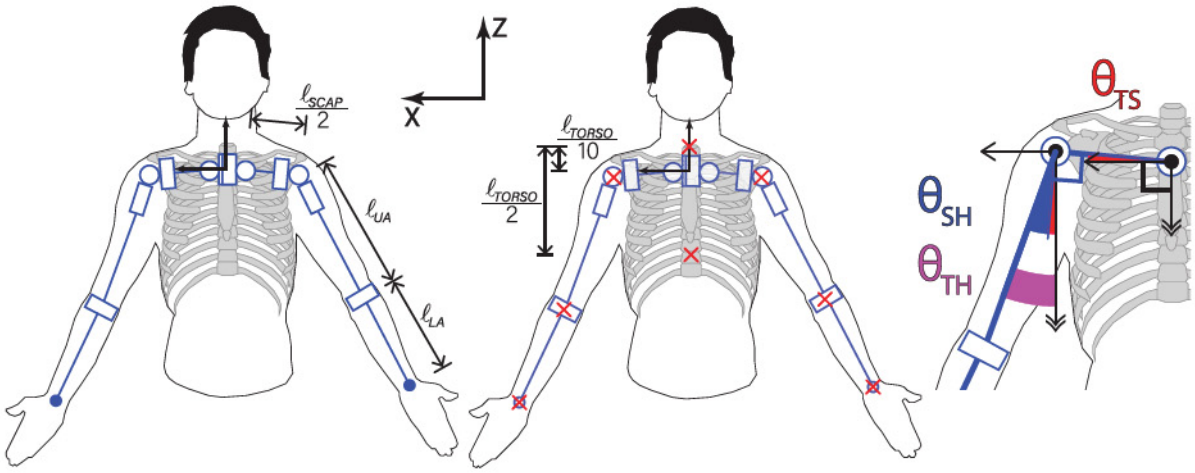

Fig. 1. Kinematic model used to enforce allometric constraints. Left: Joints and segment lengths. The scapulothoracic movement is modelled as coincident Z and Y axis rotations, with rotation of the glenohumeral joint modelled as a sequence of Z, Y, and Z rotations. The elbow is modelled as a single X rotation. Centre: Correspondence between the six landmarks estimated from the depth camera (red crosses) and their approximate anatomical locations. The Torso segment is defined by the mid-shoulder and mid-torso markers which are an allometrically scaled distance above and below the torso origin. Right: Model for capturing scapulohumeral rhythm. Scapulothoracic (θ_{TS}, red), scapulohumeral (θ_{SH}, blue), and humerothroacic (θ_{TH}, purple) are shown.

$$\mathbf{g}_{RUA,RFA} = \begin{bmatrix} \mathbf{R}_{+X} & \mathbf{q}_{\mathbf{REJC}} \\ \mathbf{0} & 1 \end{bmatrix} \tag{4}$$

where SJC and EJC are the relative positions of the shoulder and elbow joint centres in the torso and right upper arm frames respectively. The left arm is modelled in a similar manner, but with the direction of rotation reversed to allow for consistency in anatomical rotation between the two limbs.

These homogeneous transforms can be used to write the forward kinematic map $\mathcal{FK}(\mathbf{x})$. $\mathcal{FK}$ is a function that maps the system states $\mathbf{x} = [\mathbf{t}, \theta]^T$ to positions on the rigid body structure. This allows the positions of anatomical landmarks $\mathbf{p}_i$ to be found given some system state $\mathbf{x}_i$ and the local positions of these landmarks in a segment frame $\mathbf{q}_i$.

For the recovery of upper body motion, the predicted locations of the eight anatomical landmarks (Figure 1) can be written as:

$$\mathbf{p}_{torso} = \mathbf{g}_{W,T}(\mathbf{t}, \theta)\, \mathbf{q}_{torso} \tag{5}$$

$$\mathbf{p}_{RSHO} = \mathbf{g}_{W,RSC}(\mathbf{t}, \theta)\, \mathbf{q}_{RSHO} \tag{6}$$

$$\mathbf{p}_{RELB} = \mathbf{g}_{W,RUA}(\mathbf{t}, \theta)\, \mathbf{q}_{RELB} \tag{7}$$

$$\mathbf{p}_{RWRI} = \mathbf{g}_{W,RFA}(\mathbf{t}, \theta)\, \mathbf{q}_{RWRI} \tag{8}$$

with the homogenous transforms $\mathbf{g}$ found from the relative transforms (Equations 2, 3, and 4). This allows the forward kinematic map to be written as:

$$\begin{bmatrix} \mathbf{p}_{torso} & \cdots & \mathbf{p}_{LWRI} \end{bmatrix}_i = \mathcal{FK}(\mathbf{x}_i) \tag{9}$$

The anatomical landmark locations and segment dimensions (Figure 1) are estimated from the subject's standing height [28]–[32].

2) Modelling Scapulohumeral Rhythm (SHR): While the forward kinematics model presented in Equation 9 allows for independent movement of the scapula and humerus, the relative motions of these joints are coupled based on the overall position of the humerus relative to the torso. This coupled movement is known as *scapulohumeral rhythm*, and can be represented as a ratio of expected scapula-humeral motion to torso-scapula motion, and is typically taken to be 2:1 [27]. It is important to note that this ratio has been found to vary due to an added load [33], increasing the speed of the motions [34], and due to fatigue [35], with ratios ranging from 1.25:1 [36] to 7.9:1 (unloaded passive range of motion) [35].

In order to capture some of the features of SHR in the proposed model, the angles used to parameterise the transforms $\mathbf{g}_{T,SC}$ and $\mathbf{g}_{SC,UA}$ are expressed as fractions of the total torso-humeral angle θ_{UA}. Although this is a simplified model of the complex shoulder motions, the 2:1 ratio is commonly used and is a first approximation for this proposed modelling method.

The underlying abduction-adduction of the shoulder can therefore be represented by:

$$\theta_{TS} = \begin{cases} 0 & \text{for } \theta_{TH} < 45^\circ \\ \frac{1}{3}(\theta_{TH} - 45^\circ) & \text{for } \theta_{TH} \geq 45^\circ \end{cases}$$

$$\theta_{SH} = \begin{cases} \theta_{TH} & \text{for } \theta_{TH} < 45^\circ \\ \frac{2}{3}(\theta_{TH} - 45^\circ) + 45^\circ & \text{for } \theta_{TH} \geq 45^\circ \end{cases} \tag{10}$$

where θ_{TH}, θ_{TS}, and θ_{SH} are the humerothoracic, scapulothoracic, and glenohumeral elevations (Figure 1 right). A similar model is used for the protraction-retraction of the scapula and humerus, where the 2:1 ratio is still used, but without the 45° offset.

While the centre of rotation of the scapula does not occur at mid-line [37], this model is designed to be a first approximation for capturing shoulder movement. As such this removes the necessity of finding an additional allometric relationship for the mediolateral centre of rotation of the scapula.

3) Kinematic Recovery: This rigid body model was used to estimate the joint angles corresponding to the observed joint centres. This was formulated as a non-linear least squares (NLS) problem, enforcing the fixed limb length and joint range of motion constraints. Given a single Kinect observation k of anatomical landmarks y_k, the model states x_k that best fit these observations can be found via the optimisation problem:

$$\begin{aligned} \underset{\mathrm{x}_k}{\arg\min} \quad & \|\mathrm{y}_k - \mathcal{FK}(\mathrm{x}_k)\|_2^2 \\ \text{subject to:} \quad & \underline{\mathrm{x}} \leq \mathrm{x}_k \leq \overline{\mathrm{x}} \end{aligned} \tag{11}$$

where $\mathcal{FK}$ is the forward kinematic map, and $\underline{\mathrm{x}}$, $\overline{\mathrm{x}}$ are bounds on the system states that are used to keep joint angles within a physiologically consistent range.

As the kinematic recovery process is performed on each frame separately, this approach can be parallelised decreasing the time needed for computation.

B. Motions and Measures

The proposed method for obtaining an improved estimate of upper limb function is evaluated on two upper-limb assessments. The *reachable workspace* measure is designed to assess the limits to gross range of motion, while the *proximal function* measure is designed to assess the ability of the subject to perform self care activities such as feeding, grooming, and toileting. These motions are performed while seated, with guidance from an instructional video keeping the timing and order of actions consistent between trials and study sites.

1) Reachable Workspace (RW): The reachable workspace measure is performed for each arm separately from a seated position. Subjects are asked to move with their out-stretched arm through several planes of movement (Figure 2). The movements of the wrist relative to the shoulder centre are projected onto an allometrically-scaled sphere. The projected area is used as a quantitative measure of shoulder function. A full description of this method is given by [17], [38].

2) Proximal Function (PF): In contrast to the distal assessment of reach found by the RW measure, the proximal function measure assesses a person's abilities to reach key anatomical landmarks. Subjects are asked to move the tested arm to each landmark in series while seated (Figure 3). In cases where the landmark is not part of the original Kinect model (back pocket, stomach, etc.), an allometrically scaled model of these locations in the torso frame is used. The distance between the tested wrist and each landmark is measured. If the wrist is below a pre-set threshold, that landmark is said to be reached at that instant. The total duration of time that the hand is at each landmark can therefore be used as a quantitative assessment of their ability to move and hold their arm at each landmark.

III. Experimental Validation

A convenience sample of ten subjects (6F/4 M, 27.3 ± 3.1yrs., 1.70 ± 0.11 m) were recruited under informed consent (UCB IRB: 2016-01-8261). The cohort did not have any upper limb impairment, a history of upper limb surgery, nor an injury to the upper limbs within the prior six months. Subjects were asked to wear athletic clothing and sat on a chair which was adjusted so that the thigh ran parallel with the ground. A single Microsoft Kinect for Xbox One (Kinect v2) depth camera was positioned 300 cm in front of the subject, and 130 cm off the ground. A computer monitor was placed just under the camera, and used to present the instructional video for the RW and PF measures. The instructional video was initially shown to the subject to demonstrate the action. Subjects were then asked to follow each video three times for each arm for both the RW and PF movement protocols.

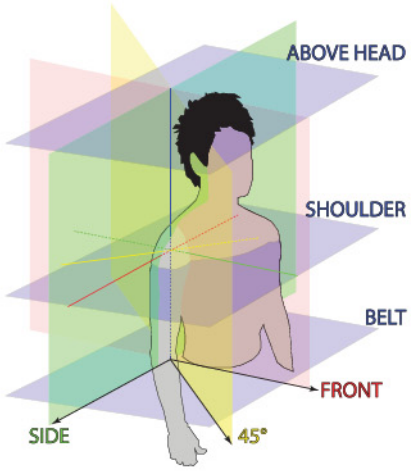

Fig. 2. Reachable workspace motions. In the RW protocol, subjects are instructed to move with their arm as straight as possible, through several planes. Each movement moves through the maximal volitional range of motion on each plane with the elbow only bending when crossing the torso. Subjects move their arm through three planes about the cranial-caudal axis in front, at 45 degrees, and to the side of the subject. Subjects are also asked to move their arm though three planes normal to the ground at the belt and shoulder levels, and above their head. The position of the wrist relative to the shoulder can then be projected on to a sphere providing a surface area metric of reaching [17], [38].

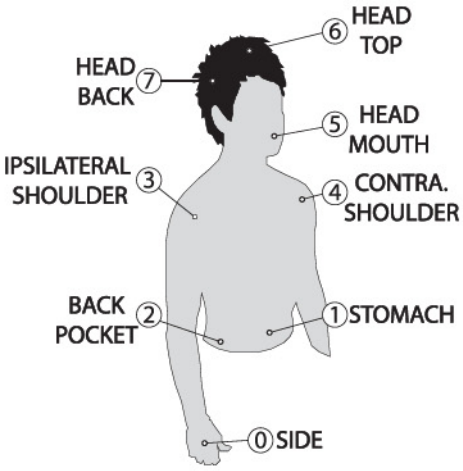

Fig. 3. Proximal function targets. In the PF protocol, subjects are instructed to move the tested hand to discrete anatomical landmarks in sequence. Starting with their hand resting by their side, they are asked to move their hand to their stomach, back-pocket, ipsi-and contra- lateral shoulders, mouth, top and back of their head, before returning their hand to their side. A delay of three seconds is given between each command.

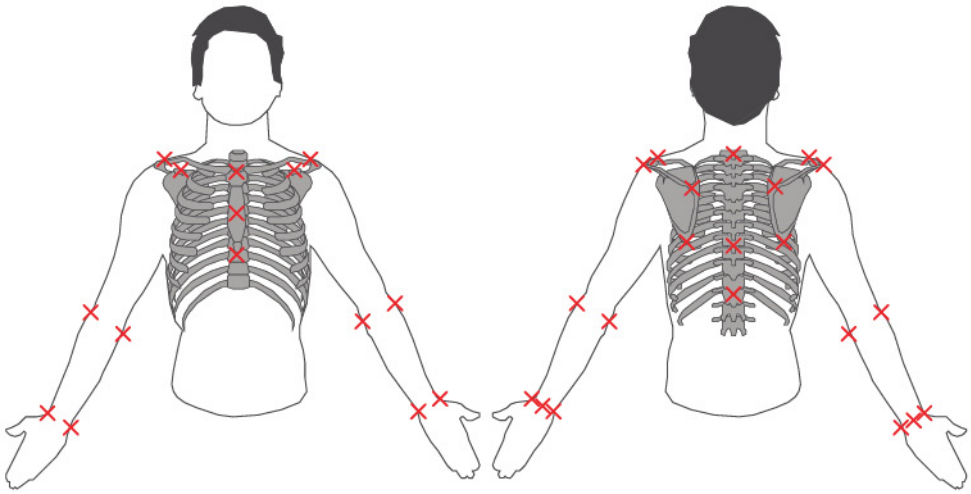

Fig. 4. Placement of active motion capture markers (red crosses) for validation. Markers were placed on the skin on palpable anatomical landmarks on the torso, scapula, elbow, and wrist [7], [39]–[41].

A. Baseline Model

In addition to the Kinect measurements, an eight camera, twenty six marker, active motion capture setup (*Phasespace*) was used as an independent measure of the torso and upper limbs. The torso and scapulae were modelled as floating bodies, with the upper arm and forearm modelled as serial chains connected to their respective scapula. This approach removed any underlying assumptions on the movement of the scapula relative to the torso, in contrast to the assumed scapula-humeral rhythm used in the constrained model (Section II-A2).

Markers were placed at common anatomical landmarks, with an additional marker placed midway between the suprasternal notch and xiphoid process (Figure 4). This allows for rigid body recovery in cases where the xiphoid process is occluded by clothing. Three markers were placed on the C7, T8, and T12 spinous processes. The markers on the scapulae were based on the standard trigonum spinae, angulus acromialis, and angulus inferior placements which can be used to define a scapula reference frame [7], [39]–[41]. Two additional markers were added at the acromioclavicular joint, and processus coracoideus to improve robustness in cases of marker occlusion [42]. Markers were also placed at the medial and lateral epicondyles of the humerus, and the processes of the radial and ulnar styloids. A final marker was placed between the radial and ulnar styloids on the dorsal side of the hand.

The instantaneous transforms for the floating segments (torso and scapulae) were computed for each frame using NLS performing an initial parameter fit to identify a marker model and a state estimateor to identify the transform for each frame. This process was repeated to find functional shoulder and elbow joint centres for each arm. The recovered functional centres were compared to allometric and landmark based methods. The markers and their corresponding anatomical locations are shown in Figure 4.

B. Implementation

All code was implemented in MATLAB, with the NLS optimisations performed in parallel using the parallel computing toolbox. To decrease the effect of erroneous readings, the raw joint centre estimates from the Kinect were pre-processed using a fifth order 1D median filter on the X, Y, and Z coordinates. Both the raw joint centre estimates from the Baseline (BR) and Kinect (DR) sensors were processed through the same rigid body model to obtain constrained Baseline (BC) and Kinect (DC) joint centre estimates.

The RW computation was performed on all four sets of joint centre trajectories as described in [17]. For the PF action, a second order, 1 Hz low-pass Butterworth filter was used to smooth the estimated distance between the tested wrist and each target location.

IV. Results

Representative motion traces for the RW and PF tests are shown in Figures 5 and 6. The signal-to-noise ratios (SNR) of the raw and constrained movement trajectories are shown in Table I. The mean percentage error of the reachable workspace test is shown in Table II, with the concordance correlation coefficients shown in Table III. Table IV shows the mean percentage errors for the proximal function test. Each of the tests are examined separately, with analysis of the estimated joint positions and the final metrics.

A. Reachable Workspace

Figure 5 shows the movement traces of the wrist during the reachable workspace action. Both the raw and processed baseline positions perform well throughout the entire movement. The raw and processed depth camera trajectories match the baseline data through the majority of the workspace. The raw depth camera diverges from the baseline at the extremes of the workspace: when the wrist moves across or behind the body. These effects appear to be reduced using the proposed model, improving consistency throughout the movement.

Table I shows the SNRs for the baseline and depth camera trajectories. The two baseline trajectories exhibit high SNR ($\geq$ 20) for both the left and right arms. This performance is lower, but acceptable (10–20), in the spine and shoulder Z directions.

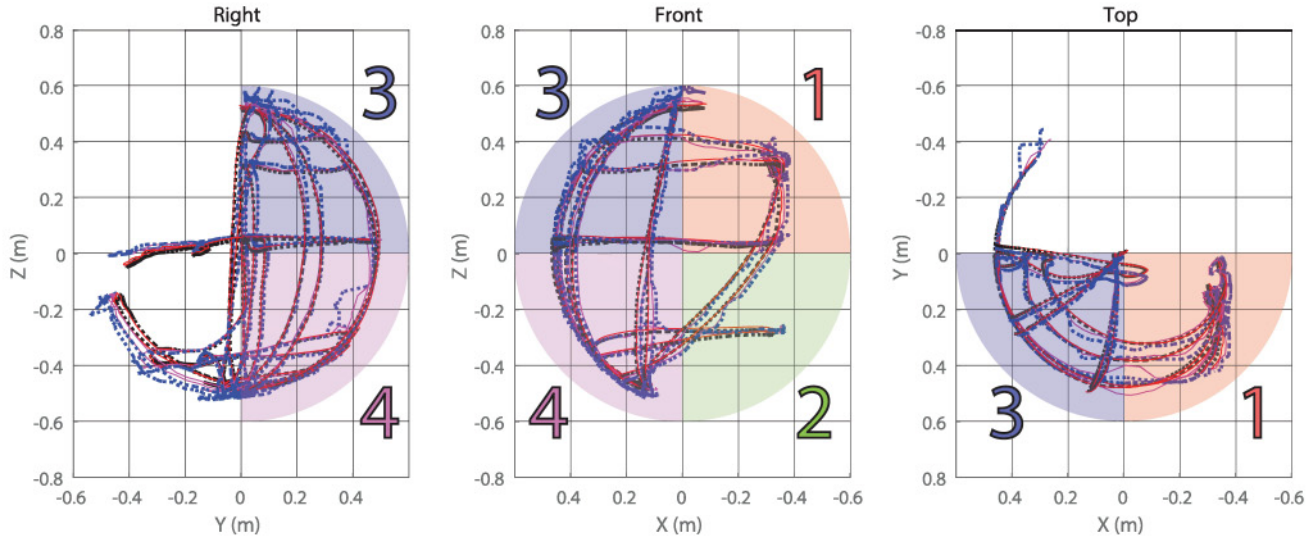

Fig. 5. Representative traces from a right reachable workspace test. Movements of the wrist are shown, with the origin centred at the mean GH shoulder position. Dotted black and blue lines are the positions of the wrist from the raw baseline and raw depth camera sensors respectively. These are filtered using the proposed rigid body model to give the solid red and purple trajectories. The four reachable workspace quadrants are highlighted with the medial above shoulder (quadrant 1) shown in red, medial below shoulder (quadrant 2) in green, lateral above shoulder (quadrant 3) shown in blue, and lateral below the shoulder (quadrant 4) shown in purple respectively. For clarity, only the data from the right, front, and top hemispheres are plotted, with the opposite hemisphere hidden.

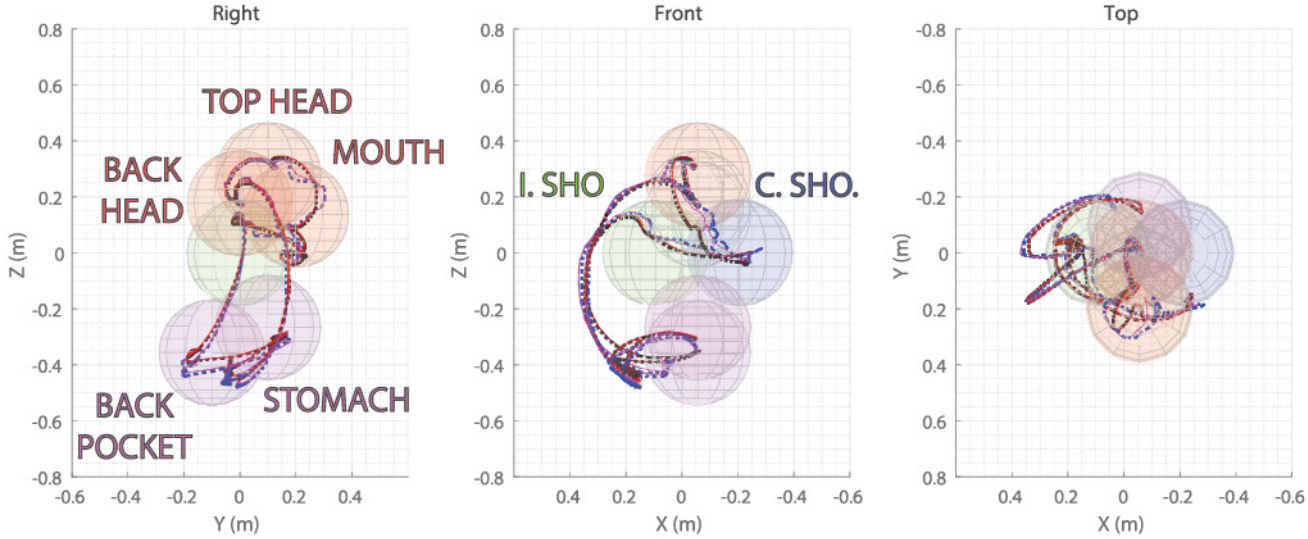

Fig. 6. Representative traces from a right proximal function test. Movements of the wrist are shown, with the origin centred at the mean GH shoulder position. Dotted black and blue lines are the positions of the wrist from the raw baseline and raw depth camera sensors respectively. These are filtered using the proposed rigid body model to give the solid red and purple trajectories. Each proximal function landmark is shown as a sphere with the radius corresponding to the threshold value of one hand length.

The raw depth camera trajectories (DR) have lower SNR across joints and axes. This decrease is more pronounced in the mid-spine and ipsilateral GH joint, where the Z axis SNR decreases below 10. The processed depth camera trajectories (BR) have higher mid-spine and ipsilateral GH SNR compared to the raw depth camera data, though these improvements are still below that of the raw baseline trajectories.

The percentage error in the corresponding reachable workspace area scores are presented in Table II. The processed baseline data has low percentage error ($\leq 5\%$) for all four quadrants and the total area. In contrast, the raw depth camera errors are higher in all quadrants with the percentage errors in the range of 4% to 26%. The constrained depth camera data has lower errors, particularly in quadrants 2 to 4, with a corresponding decrease in the quadrant totals.

The concordance between the different scores are presented in Table III. The processed baseline scores were found to have excellent concordance (≥ 0.75) when compared to the raw baseline data. The raw depth camera areas were found to have poor (<0.4) and fair ($0.4-0.59$) concordance for the left arm, and fair and

TABLE I

SIGNAL TO NOISE RATIOS IN JOINT CENTRE POSITIONS COMPARED TO THE CONSTRAINED BASELINE (BC) JOINT CENTRE TRAJECTORIES. SNR VALUES ARE SHOWN FOR EACH COORDINATE SEPARATELY, AND FOR BOTH THE LEFT AND RIGHT HAND REACHABLE WORKSPACE (RW) AND PROXIMAL FUNCTION (PF) TESTS. SNRS FOR THE RAW BASELINE (BR), RAW KINECT (DR), AND PROCESSED KINECT (DC) ARE SHOWN. COORDINATES ARE GIVEN IN THE WORLD FRAME- X FROM LEFT TO RIGHT, Y POSTERIOR TO ANTERIOR, AND Z CAUDAL TO CRANIAL. CASES WHERE THERE IS A TWO DB OR MORE DIFFERENCE BETWEEN THE RAW AND CONSTRAINED DEPTH CAMERA VALUES ARE HIGHLIGHTED WITH THE HIGHER SNR IN BOLD

		Left RW			Right RW			Left PF			Right PF		
Segment	**Axis**	**BR**	**DR**	**DC**	**BR**	**DR**	**DC**	**BR**	**DR**	**DC**	**BR**	**DR**	**DC**
Spine Shoulder	**X**	21	22	21	19	23	22	20	24	24	19	25	25
	Y	15	12	**15**	17	15	16	17	16	**18**	18	17	**20**
	Z	12	11	11	10	11	12	12	11	12	10	12	**14**
Spine Mid	**X**	19	**19**	17	17	18	18	18	**20**	18	17	**21**	19
	Y	20	9	8	25	9	9	23	15	14	26	12	12
	Z	13	5	**9**	12	5	**10**	13	6	**11**	13	5	**13**
Ipsilateral GH	**X**	20	18	19	29	18	**20**	20	19	**23**	19	19	**23**
	Y	15	12	11	19	12	12	18	**14**	12	22	16	15
	Z	12	5	**10**	15	6	**10**	11	7	**10**	15	8	**11**
Ipsilateral Elbow	**X**	26	17	**19**	27	15	14	25	15	**17**	24	14	14
	Y	24	14	15	29	12	12	24	15	**17**	28	15	15
	Z	25	15	16	30	15	15	25	15	**18**	29	**14**	11
Ipsilateral Wrist	**X**	31	20	**22**	30	17	18	29	15	**17**	30	15	16
	Y	31	15	16	32	15	15	29	11	12	31	12	13
	Z	31	18	19	30	17	17	32	20	21	31	18	19
Contralateral GH	**X**	20	22	21	21	21	22	20	24	23	21	21	**24**
	Y	20	13	13	21	15	14	23	12	13	21	16	16
	Z	14	10	**12**	10	12	13	13	10	**15**	10	12	**15**

TABLE II

MEAN ERRORS FOR THE REACHABLE WORKSPACE TEST, PRESENTED AS PERCENTAGE ERRORS FROM THE RAW BASELINE DATA. PERCENTAGE MEAN ERRORS ARE SHOWN FOR THE LEFT AND RIGHT HAND REACHABLE WORK-SPACE (RW) AND PROXIMAL FUNCTION (PF) TESTS, AND THE RAW BASELINE (BR), RAW KINECT (DR), AND CONSTRAINED KINECT (DC) ARE SHOWN. QUADRANT 1 IS MEDIAL ABOVE THE SHOULDER, QUADRANT 2 IS MEDIAL BELOW THE SHOULDER, QUADRANT 3 IS LATERAL ABOVE THE SHOULDER, AND QUADRANT 4 IS LATERAL BELOW THE SHOULDER. CASES WHERE THERE IS A 3 OR MORE PERCENT DIFFERENCE BETWEEN THE RAW AND CONSTRAINED DEPTH CAMERA VALUES ARE HIGHLIGHTED WITH THE LOWER VALUE IN BOLD

	LRW			RRW		
Quadrant	**BC**	**DR**	**DC**	**BC**	**DR**	**DC**
1: Medial Above Shoulder	6.5 ± 8.8	24.6 ± 20.1	$\mathbf{18.9 \pm 13.5}$	2.7 ± 13.2	25.6 ± 24.2	$\mathbf{18.7 \pm 18.4}$
2: Medial Below Shoulder	1.6 ± 10.3	4.4 ± 21.2	4.7 ± 17.4	2.4 ± 9.9	7.3 ± 22.2	7.6 ± 23.3
3: Lateral Above Shoulder	1.9 ± 8.0	11.8 ± 13.4	$\mathbf{5.5 \pm 8.4}$	0.7 ± 9.4	7.3 ± 12.2	$\mathbf{2.6 \pm 10.3}$
4: Lateral Below Shoulder	0.3 ± 8.3	8.2 ± 15.4	$\mathbf{4.0 \pm 9.9}$	1.1 ± 10.0	5.3 ± 12.4	$\mathbf{2.1 \pm 10.4}$
Total	2.4 ± 8.1	12.0 ± 15.0	$\mathbf{7.8 \pm 9.8}$	1.4 ± 9.9	9.4 ± 12.3	5.6 ± 10.5

TABLE III

LIN'S CONCORDANCE CORRELATION COEFFICIENTS FOR THE REACHABLE WORKSPACE TEST COMPARED TO THE RAW BASELINE DATA. HIGHEST CCC VALUE BETWEEN THE RAW AND CONSTRAINED DEPTH CAMERA VALUES ARE HIGHLIGHTED IN BOLD

	LRW			RRW		
Quad.	**BC**	**DR**	**DC**	**BC**	**DR**	**DC**
1	0.85	0.31	**0.53**	0.89	0.69	**0.79**
2	0.78	0.07	**0.39**	0.92	0.49	**0.52**
3	0.86	0.58	**0.83**	0.82	0.68	**0.77**
4	0.83	0.43	**0.77**	0.81	0.62	**0.76**
Total	0.81	0.36	**0.69**	0.80	0.64	**0.76**

good $(0.6 - 0.74)$ concordance with the right arm. In contrast, the concordance is higher for the processed depth camera, with quadrants 3 and 4 and the total areas having good/excellent scores.

B. Proximal Function

The wrist trajectories for the proximal function test are shown in Figure 6. The raw and constrained baseline trajectories overlap throughout the test and across all landmarks. Both the raw and constrained depth camera trajectories are close to baseline for most targets, though error is seen for the back pocket, contralateral shoulder, and mouth targets. The processed depth camera trajectories appear smoother, especially at these higher error targets.

The SNRs shown in Table I show a similar pattern to the reachable workspace test. SNRs are high between the raw and processed baseline data, with decreases seen in the raw depth camera joint positions. The constrained depth camera data exhibits higher SNR compared to the raw depth camera data, particularly in the Z direction for the GH joints and the mid-spine.

The mean percentage errors in target duration for each of the different methods are presented in Table IV. All methods show low percentage error ($< 5\%$) for the torso landmarks. The error increases dramatically for the head landmarks, with the back of head target being extremely inconsistent. To aid analysis, the three head targets were combined to provide a *head total* metric. The duration that the hand was found to be at all head targets was found to have low mean percentage error ($< 5\%$). These low errors correspond to estimated target durations that were within $0.1\ s$ for the torso and shoulder targets for all methods. The head total metric was found to agree between the two raw methods

TABLE IV
MEAN PERCENTAGE ERROR IN DURATION FOR THE PROXIMAL FUNCTION MEASURE. TARGET DURATION ESTIMATED FROM THE CONSTRAINED BASELINE (BC), RAW DEPTH CAMERA (DR), AND CONSTRAINED DEPTH CAMERA (DC) ARE COMPARED AGAINST THE RAW BASELINE (BR) DURATION

	LPF			RPF		
Quadrant	**BC**	**DR**	**DC**	**BC**	**DR**	**DC**
Stomach	-0.2 ± 4.1	-0.8 ± 0.9	-0.1 ± 4.3	-3.7 ± 18.9	-0.3 ± 1.1	-0.3 ± 2.9
Back Pocket	-1.9 ± 3.9	0.8 ± 1.7	-1.8 ± 3.3	-4.5 ± 3.9	-0.1 ± 2.1	-4.0 ± 3.8
Ipsi. SHO	0.5 ± 2.6	0.0 ± 1.1	-0.7 ± 2.6	-0.4 ± 2.4	-0.2 ± 0.6	-1.8 ± 1.8
Contra. SHO	2.6 ± 1.7	0.3 ± 1.3	5.1 ± 11.4	4.4 ± 4.5	0.6 ± 1.5	4.9 ± 4.9
Head Mouth	10.9 ± 52.5	2.4 ± 28.1	2.9 ± 42.2	21.3 ± 74.7	-7.2 ± 21.3	12.9 ± 63.8
Head Top	-34.1 ± 56.4	-0.9 ± 49.6	-33.9 ± 56.5	-24.1 ± 65.2	8.6 ± 24.6	-13.5 ± 63.8
Head Back	X	-21.7 ± 81.8	X	X	X	X
Head Total	-2.6 ± 12.2	-0.1 ± 0.5	-3.5 ± 12.7	-0.7 ± 0.8	-0.3 ± 0.6	-0.9 ± 1.0

(< 0.1 s), and between the two processed methods (< 0.1 s), though the raw and processed methods were found to not be consistent between each other with a difference of 0.3 s between the totals.

V. DISCUSSION

A. Reachable Workspace Measure

The results presented in Section IV-A support the use of both the proposed rigid body model for post-processing motion data, and support the use of depth cameras to perform the reachable workspace assessment. The excellent concordance and low mean percentage error between the raw and constrained baseline data suggests that the proposed rigid-body model is appropriate for modelling the reachable workspace movements. The low percentage error and good/excellent concordance seen in quadrants 3 and 4 suggest that the constrained depth camera data is suitable for use as a performance metric.

Quadrants that correspond to self-occluding movements (1 and 2) exhibit higher percentage error, and lower concordance. This is likely due to the limitations of using a single depth camera for this application. As the tested limb moves in front of the subject, the instantaneous estimates of the occluded joint centre positions are likely to become worse. This is supported by the low SNR seen at the ipsilateral GH joint. This effect is compounded by the need for the elbow to bend during the medial arm movements. This reduces the maximal area during reaching in quadrants 1 and 2 (as seen in the Front and Top views of Figure 5. Increased error in tracking the elbow bend, and an overall decrease in area could both disproportionately increase the percentage mean error in these quadrants. The addition of rigid body constraints reduces this effect resulting in improved SNR, lower mean percentage error, and concordance of the final reachable workspace area.

The low error ($< 5\%$) and excellent concordance between the baseline and processed depth camera measures in quadrants 3 and 4 suggest that these quadrants may be the most appropriate for clinical assessment. The lower mean percentage error and higher concordance seen for the total area metric should be treated with caution. As quadrants 3 and 4 are likely to have a larger areas than quadrant 2, the improved performance in total area may be based on improvements in the quadrant 3 and 4 sub-scores.

B. Proximal Function Measure

The results presented in Section IV-B support the use of depth cameras for assessing proximal function, though at a coarser spatial resolution than initially planned. As only the wrist does not move significantly between the mouth, top, and back of head positions, these three targets have to be merged into a single head target.

The benefit of using the proposed rigid-body-model for the PF test is less clear, with signs that it may introduce a systematic error. The mean percentage errors for both constrained methods are higher than their raw counterparts for the back pocket, contra-lateral shoulder, and head positions. This systematic error is likely to be caused by a combination of self occlusion and scapular movement that does not match the model used in Section II-A2. In the raw methods, the target landmarks are based on a rigid body model that only incorporates the estimated locations of the left, right, and mid shoulders and the mid-spine. In contrast, the constrained methods use all of the observed joint estimates, including the elbows and wrists of both arms. The addition of these joint centres may decrease the overall pose estimate due to multiple erroneous estimates of joint position.

Despite the differences in the duration measured by the raw and constrained methods, this duration metric does seem feasible for assessing proximal function. Performance could be improved by reducing this metric into a binary value by comparing the measured duration to a preset threshold, similar to other clinical scores. Extensions to determine improvement to the PF test are included in Section VI-B.

It is interesting to note how the addition of a rigid body model was of benefit to the RW protocol, but may introduce error into the PF protocol. It is likely that this is due to a fundamental difference in how these protocols function. In RW, the accuracy of the GH centre is important as the GH metrics are all based on the relative positions of the wrist and the shoulder centre. As the rigid body model allows for improved estimates of position by constraining limb lengths and adding in scapular-humeral rhythm, there is a corresponding improvement in the estimated RW areas when compared to the raw depth camera trajectories. This improvement is highlighted at the extremes of the workspace. When the arms are outstretched above or behind the subject, the skeletonisation algorithm used by these cameras may have difficulty identify consistent shoulder positions. By anchoring the shoulder position to landmarks that are more

consistent at these times (contralateral shoulder and torso), these constraints improve the accuracy of the joint centres. Furthermore, the SHR model used in Section II-A2 is based on relatively pure arm abduction. This is similar to the arm movements seen in the RW quadrants 3 and 4, potentially resulting in improved correlation and lower mean percentage errors. In contrast, the cross body motions required in the RW quadrants 1 and 2 may be dissimilar to the movement pattern assumed by the model resulting in higher errors and lower concordance.

In contrast, the PF measure measures the time that the wrist is near each anatomical landmark. While the error in the ipsilateral GH joint centre position decreases using the rigid body model this does not result in an improvement in the estimated duration that the hand was at each target. This may be due to two factors, the choice of assessment metric, and the underlying model assumptions. The duration metric was chosen as it should be robust to the different strategies used by subjects when they reach each target. As there are a number of different ways a subject could reach their shoulder, measuring the duration of time that the wrist is one hand's length from each target is a convenient assessment of function. This metric only depends on the pose of the torso and the relative position of the wrist. In cases of self occlusion, the addition of rigid body constraints and an explicit SHR may introduce artefacts in positions of the wrist and torso. This explains the consistency between the two raw and two processed measures, with a consistent offset between each measure. In this case, adding constraints on the torso by either reducing the expected movement, or adding in landmarks (such as the hips) could reduce these effects.

C. Clinical Applicability

This paper indicates the potential for the RWS and PF measures to provide a quantitative measure of upper limb movement and function. The repeatability and accuracy of these measures indicate their viability for tracking changes in function due to pathology or treatment. The total time required to perform both tests on both limbs is under four minutes, allowing for integration into existing clinical workflows and requiring minimal supervision and expertise to conduct the test. As the observed movements are stored after each test, reference motions can be presented to subjects as part of patient education or to highlight changes in function. The motion paths and joint angles obtained during these tests allow for analysis of movement synergies and stereotyped motion patterns. This suggests the clinical utility of this approach, providing measures that can be used for assessment and tracking immediately, while allowing for the development of new metrics based on aggregating patient cohorts. These additional measures would provide insight on the degree of compensation and the presence of movement synergies, two key factors for the accurate assessment of individuals with neuromusculoskeletal conditions.

VI. Summary

This paper introduced and assessed two upper limb functional assessments that can be used clinically with a depth camera. The effect of adding a rigid body model to raw estimates of joint centre was assessed. These initial tests suggest that both assessment measures can be performed on individuals without upper limb impairment and that these measures are accurate when compared to a baseline motion capture system.

For the RW measure, it is recommended that a rigid body model is used to improve the accuracy of the resulting areas. Investigators should also note that quadrants 3 and 4 may be less susceptible to errors due to self occlusion.

The proposed duration measure for PF also appears to be a feasible measure for assessing subjects, though there is insufficient evidence to accept or reject the use of the rigid body model. Further testing is needed with individuals with limitations in upper limb function to determine if these models are beneficial, if the models needs to be changed for these populations, or if the variations seen in this study can simply be neglected by comparing the duration to a pass/fail threshold.

A. Limitations

While this paper shows the initial feasibility of using these methods, testing was limited to ten people without any upper limb impairment. To determine if these measures are able to quantify and distinguish varying levels of function, these tests should be repeated for a larger cohort with varying levels of ability.

There are also limitations due to the methods and sensor choice. Depth camera systems are limited by a single viewpoint, making them sensitive to self-occlusion. The algorithms used to perform the initial joint centre estimation may also be sensitive in cases where the upper limbs are close to the torso, increasing joint centre error. The scapular-GH model used in this work may not be appropriate for individuals with shoulder dysfunction, or individuals who have undergone shoulder surgery. Additional study of specific clinical cohorts is needed to determine the efficacy and to assess the effect of each of these limitations.

B. Future Work

To determine the clinical utility of these methods, additional testing will be performed on individuals with varying degrees of musculoskeletal function specificially investigating individuals with shoulder replacement and muscular weakness/dystrophy. To reduce any errors in unrealistic rotation of the torso, the hip joint centres from the depth camera could be added, or additional rotational constraints can be placed on torso movement. True movement of the torso could also be reduced by providing a hard-backed chair, with subjects being coached to keep their back in contact. An Unscented Kalman Filter [43] could be used to reduce high frequency noise in the joint angles by adding dynamic constraints to the recovered motion. The addition of this filtering step should be treated with caution though as it is a sequential processing method which will prevent the parallelisation of the kinematic recovery step.

Acknowledgment

The authors would like to thank Jeannie Bailey, Brian Feeley, Oliver O'Reilly, and Alina Nicorici for their assistance and guidance in this work.

REFERENCES

[1] J. See *et al.*, "A standardized approach to the Fugl-Meyer assessment and its implications for clinical trials," *Neurorehabilitation Neural Repair*, vol. 27, no. 8, pp. 732–741, 2013.

[2] C. Bushnell *et al.*, "Chronic stroke outcome measures for motor function intervention trials: Expert panel recommendations," *Circulation: Cardiovascular Quality Outcomes*, vol. 8, no. 6_suppl_3, pp. S163–S169, 2015.

[3] W. M. Shumway-Cook A, *Motor control: Translating research into clinical practice*. Philadelphia, PA, USA: Lippincott Williams & Wilkins, 2017.

[4] M. Demers and M. F. Levin, "Do activity level outcome measures commonly used in neurological practice assess upper-limb movement quality?" *Neurorehabilitation Neural Repair*, vol. 31, no. 7, pp. 623–637, 2017.

[5] D. A. Winter, "Kinematics," in *Biomechanics and Motor Control of Human Movement*, Hoboken, NJ, USA: Wiley, 2009.

[6] S. S. H. U. Gamage and J. Lasenby, "New least squares solutions for estimating the average centre of rotation and the axis of rotation," *J. Biomechanics*, vol. 35, no. 1, pp. 87–93, 2002.

[7] M. Lempereur, F. Leboeuf, S. Brochard, J. Rousset, V. Burdin, and O. Rémy-Néris, "In vivo estimation of the glenohumeral joint centre by functional methods: Accuracy and repeatability assessment," *J. Biomechanics*, vol. 43, no. 2, pp. 370–374, 2010.

[8] M. Jackson, B. Michaud, P. Tétreault, and M. Begon, "Improvements in measuring shoulder joint kinematics," *J. Biomechanics*, vol. 45, no. 12, pp. 2180–2183, 2012.

[9] J. McConnell, C. Donnelly, S. Hamner, J. Dunne, and T. Besier, "Passive and dynamic shoulder rotation range in uninjured and previously injured overhead throwing athletes and the effect of shoulder taping," *PM R*, vol. 4, no. 2, pp. 111–116, 2012.

[10] R. L. Lawrence, A. M. Ellingson, and P. M. Ludewig, "Validation of single-plane fluoroscopy and 2D/3D shape-matching for quantifying shoulder complex kinematics," *Medical Eng. Phys.*, vol. 52, pp. 69–75, 2018.

[11] Q. Wang, G. Kurillo, F. Ofli, and R. Bajcsy, "Evaluation of pose tracking accuracy in the first and second generations of microsoft Kinect," in *Proc. IEEE Int. Conf. Healthcare Informat.*, pp. 380–389, 2015.

[12] Z. Zhang, "Microsoft Kinect sensor and its effect," *IEEE Multimedia*, vol. 19, no. 2, pp. 4–10, Apr. 2012.

[13] A. Pfister, A. M. West, S. Bronner, and J. A. Noah, "Comparative abilities of Microsoft Kinect and Vicon 3D motion capture for gait analysis," *J. Med. Eng. Technol.*, vol. 38, no. 5, pp. 274–280, 2014.

[14] S. Choppin, B. Lane, and J. Wheat, "The accuracy of the Microsoft Kinect in joint angle measurement," *Sports Technol.*, vol. 7, no. 1-2, pp. 98–105, 2014.

[15] B. Bonnechère *et al.*, "Validity and reliability of the Kinect within functional assessment activities: Comparison with standard stereophotogrammetry," *Gait Posture*, vol. 39, no. 1, pp. 593–598, 2014.

[16] A. Fernández-Baena, A. Susín, and X. Lligadas, "Biomechanical validation of upper-body and lower-body joint movements of kinect motion capture data for rehabilitation treatments," in *Proc. 4th Int. Conf. Intell. Netw. Collaborative Syst.*, 2012, pp. 656–661.

[17] G. Kurillo, A. Chen, R. Bajcsy, and J. J. Han, "Evaluation of upper extremity reachable workspace using Kinect camera," *Technol. Health Care*, vol. 21, no. 6, pp. 641–656, 2013.

[18] J. J. Han, G. Kurillo, R. T. Abresch, E. de Bie, A. Nicorici, and R. Bajcsy, "Reachable workspace in facioscapulohumeral muscular dystrophy (FSHD) by kinect," *Muscle Nerve*, vol. 51, no. 2, pp. 168–175, 2015.

[19] J. J. Han, E. De Bie, A. Nicorici, R. T. Abresch, R. Bajcsy, and G. Kurillo, "Reachable workspace reflects dynamometer-measured upper extremity strength in facioscapulohumeral muscular dystrophy," *Muscle Nerve*, vol. 52, no. 6, pp. 948–955, 2015.

[20] J. J. Han, G. Kurillo, R. T. Abresch, E. De Bie, A. Nicorici, and R. Bajcsy, "Upper extremity 3-dimensional reachable workspace analysis in dystrophinopathy using Kinect," *Muscle Nerve*, vol. 52, no. 3, pp. 344–355, 2015.

[21] J. J. Han *et al.*, "Reachable workspace and performance of upper limb (PUL) in Duchenne muscular dystrophy," *Muscle Nerve*, vol. 53, no. 4, pp. 545–554, 2016.

[22] B. Oskarsson *et al.*, "Upper extremity 3-dimensional reachable workspace assessment in amyotrophic lateral sclerosis by Kinect sensor," *Muscle Nerve*, vol. 53, no. 2, pp. 234–241, 2016.

[23] J. Clément, M. Raison, and D. M. Rouleau, "Reproducibility analysis of upper limbs reachable workspace, and effects of acquisition protocol, sex and hand dominancy," *J. Biomechanics*, vol. 68, pp. 58–64, 2018.

[24] R. P. Matthew, S. Seko, R. Bajcsy, and J. Lotz, "Kinematic and kinetic validation of an improved depth camera motion assessment system using rigid bodies," *IEEE J. Biomed. Health Informat.*, vol. 23, no. 4, pp. 1784–1793, Jul. 2019.

[25] R. P. Matthew, S. Seko, J. Bailey, R. Bajcsy, and J. Lotz, "Estimating sit-to-stand dynamics using a single depth camera," *IEEE J. Biomed. Health Informat.*, vol. 23, no. 6, pp. 2592–2602, Nov. 2019.

[26] J. Bailey *et al.*, "ISSLS PRIZE IN BIOENGINEERING SCIENCE 2019: biomechanical changes in dynamic sagittal balance and lower limb compensatory strategies following realignment surgery in adult spinal deformity patients," *Eur. Spine J.*, vol. 28, no. 5, pp. 905–913, 2019.

[27] V. T. Inman, J. B. Saunders, and L. C. Abbott, "Observations of the function of the shoulder joint," *Clin. Orthopaedics Related Res.*, vol. 330, pp. 3–12, 1996.

[28] W. T. Dempster, "Space requirements of the seated operator: Geometrical, kinematic, and mechanical aspects other body with special reference to the limbs," Michigan State Univ East Lansing, East Lansing, MI, USA, Tech. Rep. 55-159, 1955.

[29] D. B. Chaffin, G. B. J. Andersson, and B. J. Martin, "Occupational biomechanics," John Wiley & Sons, 2006.

[30] A. Tilley, *The Measure of Man and Woman: Human Factors in Design*. Hoboken, NJ, USA: Wiley, 2001.

[31] J. L. Durkin and J. J. Dowling, "Analysis of body segment parameter differences between four human populations and the estimation errors of four popular mathematical models," *J. Biomechanical Eng.*, vol. 125, no. 4, pp. 515–522, 2003.

[32] R. Dumas, L. Chèze, and J. P. Verriest, "Adjustments to McConville et al. and Young et al. body segment inertial parameters," *J. Biomechanics*, vol. 40, no. 3, pp. 543–553, 2007.

[33] Y. Kon, N. Nishinaka, K. Gamada, H. Tsutsui, and S. A. Banks, "The influence of handheld weight on the scapulohumeral rhythm," *J. Shoulder Elbow Surgery*, vol. 17, no. 6, pp. 943–946, 2008.

[34] F. Fayad, *et al.*, "3-D scapular kinematics during arm elevation: Effect of motion velocity," *Clin. Biomechanics*, vol. 21, no. 9, pp. 932–941, 2006.

[35] K. J. McQuade, S. H. Wei, and G. L. Smidt, "Effects of local muscle fatigue on three-dimensional scapulohumeral rhythm," *Clin. Biomechanics*, vol. 10, no. 3, pp. 144–148, 1995.

[36] N. K. Poppen and P. S. Walker, "Normal and abnormal motion of the shoulder," *J. Bone Joint Surgery*, vol. 58, pp. 195–201, 1976.

[37] C. Amabile, A. M. Bull, and A. E. Kedgley, "The centre of rotation of the shoulder complex and the effect of normalisation," *J. Biomechanics*, vol. 49, no. 9, pp. 1938–1943, 2016.

[38] J. Han, G. Kurillo, R. Abresch, A. Nicorici, and R. Bajcsy, "Validity, reliability, and sensitivity of a 3D vision sensor-based upper extremity reachable workspace evaluation in neuromuscular diseases," *PLOS Currents*, vol. 5, pp. 1–21, 2013.

[39] P. W. McClure, L. A. Michener, B. J. Sennett, and A. R. Karduna, "Direct 3-dimensional measurement of scapular kinematics during dynamic movements in vivo," *J. Shoulder Elbow Surgery*, vol. 10, no. 3, pp. 269–277, 2001.

[40] H. M. Vermeulen, M. Stokdijk, P. H. Eilers, C. G. Meskers, P. M. Rozing, and T. P. Vliet Vlieland, "Measurement of three dimensional shoulder movement patterns with an electromagnetic tracking device in patients with a frozen shoulder," *Ann. Rheumatic Diseases*, vol. 61, no. 2, pp. 115–120, 2002.

[41] F. Fayad *et al.*, "Three-dimensional scapular kinematics and scapulohumeral rhythm in patients with glenohumeral osteoarthritis or frozen shoulder," *J. Biomechanics*, vol. 41, no. 2, pp. 326–332, 2008.

[42] C. G. Meskers, H. M. Vermeulen, J. H. De Groot, F. C. Van Der Helm, and P. M. Rozing, "3D shoulder position measurements using a six-degree-of-freedom electromagnetic tracking device," *Clin. Biomechanics*, vol. 13, no. 4-5, pp. 280–292, 1998.

[43] S. J. Julier and J. K. Uhlmann, "New extension of the Kalman filter to nonlinear systems," *Signal Process. Sensor Fusion, and Target Recognit., VI*, vol. 3068, pp. 182–193, 1997.